



Effect of heat input on mechanical performance and corrosion behaviors of local dry underwater pulsed MIG SUS304 weldments

Zhenmin Wang¹ · Bin Zhang¹ · Haipeng Liao¹ · Xiangmiao Wu¹ · Jiyu Tian¹ · Qin Zhang²

Received: 23 May 2023 / Accepted: 1 February 2024 / Published online: 12 February 2024
© The Author(s), under exclusive licence to Springer-Verlag London Ltd., part of Springer Nature 2024

Abstract

To reveal the influence mechanism of linear heat input (LHI) on the mechanical properties and corrosion behaviors of SUS304 weldments manufactured by local dry underwater pulsed metal inert-gas welding (LDU-PMIG), phase structure, grain structure, grain preferred orientation, and grain type of weld metal (WM) were investigated in this paper. With LHI increasing, ferrite phase morphology transformed from lath to skeleton, and grain size was enlarged. The content of equiaxed grains was increased, and that of columnar grains was reduced remarkably. The mechanical performance ascended first and then reduced with the increase of LHI. The increase of equiaxed grain content and the diversification of grain preferred orientation were beneficial to the improvement of mechanical performance, then, grain coarsening led to mechanical performance decreasing. Besides, the corrosion potential, corrosion current and pitting potential of WM were detected through electrochemical corrosion tests. The results illustrated that the corrosion resistance of WM was lower than that of base metal (BM), and the corrosion rate was enlarged with LHI enhancing, which meant the corrosion resistance declining. The corrosion resistance was mainly determined by Cr precipitates, ferrite phase and grain size. The microhardness, tensile strength, and elongation reached their maxima in the LHI of 336.7 J/mm. The greatest corrosion resistance of WM was obtained in the LHI of 256.2 J/mm and reached 69.9% of BM. This study is meaningful to promote the further development and application of LDU-PMIG in marine underwater welding field.

Keywords Local dry underwater welding · Heat input · Microstructure · Mechanical performance · Corrosion behavior

1 Introduction

304 austenite stainless steel (SUS304) possesses high corrosion resistance, remarkable mechanical properties and fine weldability [1, 2], extensively utilized in the field of marine service environment, oil and gas industries, chemical and process industries, dairy industries and nuclear sector [3, 4]. The installation and maintenance of underwater SUS304 facilities required underwater welding techniques, which were mainly divided into three types: wet underwater welding, dry underwater welding, and local dry underwater

welding (LDUW). LDUW has developed rapidly in recent years under the urgent need of underwater installation and maintenance of marine facilities. Drainage devices were applied in LDUW to transport drainage gas to the local welding area, which drained the water in the welding area and formed a local dry environment filled with drainage gas. Therefore, better welding quality was achieved by LDUW compared with wet underwater welding, and LDUW exhibited more convenience and flexibility than dry underwater welding. Pulsed metal inert-gas welding (PMIG) was applied in LDUW to obtain LDU-PMIG. High welding efficiency and satisfactory weld formation quality were achieved by LDU-PMIG [5, 6]. Based on these advantages, LDU-PMIG had broad application prospects in the field of marine underwater welding.

Generally, high mechanical performance is required for underwater weldments under the influence of water pressure and water flow impact. Weldment corrosion may occur due to the existence of corrosive ions in water, furthermore, high corrosion rate may result in weld defects and performance

✉ Jiyu Tian
tianjiyu@scut.edu.cn

✉ Qin Zhang
cszhangq@scut.edu.cn

¹ School of Mechanical & Automotive Engineering, South China University of Technology, Guangzhou 510641, China

² School of Computer Science & Engineering, South China University of Technology, Guangzhou 510006, China

degradation. Therefore, to reduce the corrosion rate is also an urgent need for weldments during service. SUS304 underwater weldments were obtained by LDU-PMIG, and it has been investigated how pulse current affected the droplet transfer behavior and weld formation in our previous work [6]. However, different pulse current changed LHI, which was a key factor determining the mechanical properties and corrosion behaviors of weldments.

LHI had a significant influence on the mechanical properties of weldments. Under the condition of constant welding speed, LHI changed the cooling time of molten pools, which led to changes of weldment microstructure. Consequently, mechanical properties of weldments were changed by different LHI. Some studies have been reported to reveal the relationship between LHI and mechanical properties of on-landing welding technologies. Zhan et al. [7] reported that the tensile strength of 304 fiber-diode hybrid laser weldments displayed a trend of first increasing and then decreasing as LHI went up. Ceyhun [8] discovered that the tensile and yield strength, microhardness, and bending strength of laser weldments decreased with LHI increasing, nonetheless, the ductility and impact toughness were improved. Kumar et al. [4] proposed that gas tungsten arc welded 304 joints under higher LHI exhibited lower tensile strength and microhardness owing to grain coarsening of WM and heat affected zone (HAZ). Kumar et al. [9] studied laser dissimilar grade nickel alloys weldments, whose tensile strength and microhardness increased first and then decreased with LHI rising. Singh et al. [10] researched the impact of two different LHI on tensile behavior of martensitic stainless steel welded joints. Grain coarsening happened in higher LHI resulted in tensile strength decreasing dramatically. The impact of LHI on mechanical performance of underwater weldments has also been studied. Ma et al. [11] found that the microhardness of duplex stainless steel weldments changed little due to the mutual balance of grain coarsening and solid solution strengthening effect. Li et al. [12] revealed that the tensile strength, impact toughness and microhardness of E40 wet underwater weldments increased as LHI ascended because of the solid solution strengthening of alloying elements. Di et al. [13] uncovered that cooling rate of molten pools increased with LHI decreasing in simulated local dry underwater welding, and the weldments under lower LHI exhibited better strength and toughness due to more acicular ferrite content. Gao et al. [14] demonstrated that higher LHI promoted microstructure coarsening and increased the diffusive hydrogen content, which caused mechanical performance deteriorated in the S355 underwater wet weldments.

LHI had a vital influence on the corrosion behaviors of weldments. Different LHI made weldments obtain different phase distribution and content, grain size and precipitates content, which altered the corrosion behaviors of weldments remarkably. Studies have been finished to find the impact of

LHI on corrosion behaviors of on-landing weldments. Li et al. [15] found that the intergranular corrosion resistance decreased because of more Cr precipitates and lower $\Sigma 3$ boundaries with LHI rising. Han et al. [16] put forward that the pitting potential of duplex stainless steel tungsten inert-gas (TIG) weldments changed little under different LHI, however, the corrosion rate of weldments increased owing to the less $\Sigma 3$ coincident site lattice (CSL) content with LHI increasing. Singh et al. [10] revealed that the pitting corrosion resistance was improved under low LHI in martensitic stainless steel joints, which was mainly attributed to the less depletion of chromium. Zhang et al. [17] reported that the corrosion resistance of 304 HAZ improved with cooling time increasing. A few studies have been reported to explore the effect of LHI on corrosion behaviors of underwater weldments. Ma et al. [11] suggested that all duplex stainless steel weldments, produced by wet underwater flux-cored arc welding (FCAW), had inferior corrosion resistance to that of BM, and the corrosion resistance increased with LHI rising because of solid solution of alloying elements and lower grain boundary area per unit volume. Sun et al. [18] found that S32101 dry underwater welded joints reflected higher susceptibility to localized corrosion in high LHI, which meant the corrosion resistance reduced as LHI rose.

Mechanical properties and corrosion behaviors of different materials and welding methods have been studied currently, but now the researches about LDU-PMIG are extremely limited and it is still unknown how LHI affects the mechanical performance and corrosion behaviors of SUS304 local dry underwater weldments. This paper aims to explore the mechanical performance and corrosion behaviors of SUS304 LDU-PMIG weldments with LHI increasing. The phase structure, grain characteristics, fracture morphology and element distribution were investigated systematically. Microhardness test and tensile test were carried out to measure the mechanical performance of WM, and the corrosion behaviors and corrosion resistance were investigated through electrochemical corrosion tests. This investigate is expected to reveal the influence of LHI on the mechanical properties and corrosion behaviors of SUS304 local dry underwater weldments, which matters to the further development and application of LDU-PMIG in marine equipment field.

2 Experimental procedure

2.1 Materials and welding procedure

SUS304 plates with the dimension of 300 mm×100 mm×5 mm cut from rolled sheets were utilized as BM, and ER308LSi welding wire with the diameter of 1.2 mm was applied as the filler metal. Table 1 displays the chemical compositions of BM and filler metal.

Table 1 Chemical composition of BM and filler metal (wt.%)

Material	C	Mn	S	Si	Cr	Ni	Mo	Fe
SUS304	0.059	1.00	0.003	0.53	18.18	8.10	0.03	Bal
ER 308LSi	0.019	1.72	0.003	0.46	20.8	10.1	-	Bal

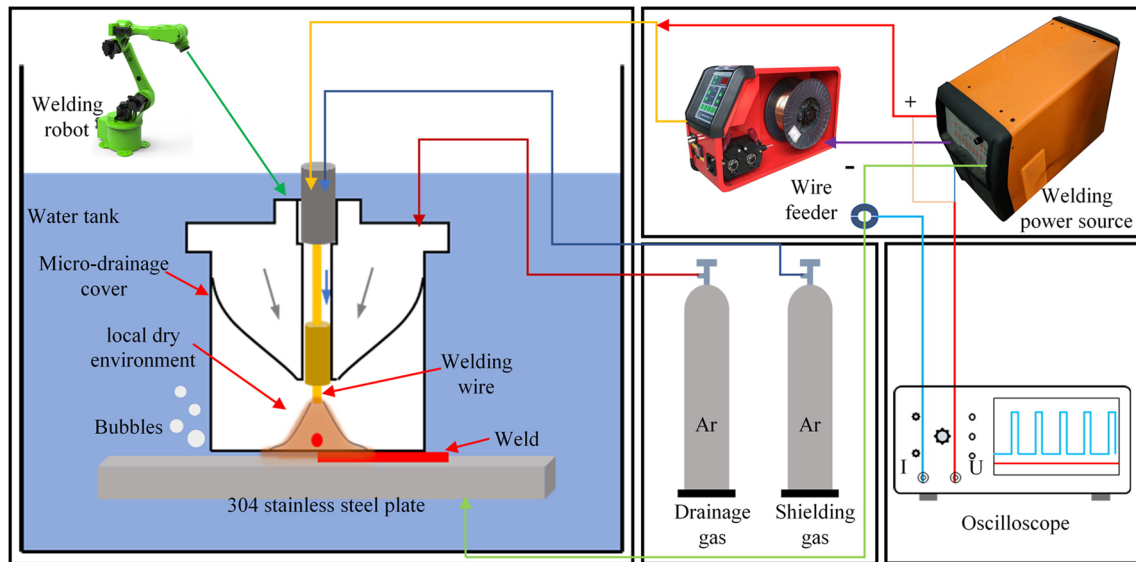


Fig. 1 Schematic diagram of LDU-PMIG welding system

SUS304 local dry underwater weldments were fabricated under different LHI by the self-developed LDU-PMIG system, as shown in Fig. 1. The system was composed of self-developed underwater welding power source, drainage cover, gas supply device, water tank, welding robot, wire feeder, and electrical signals acquisition device, etc. The electrical signals acquisition device consisted of oscilloscope, current and voltage sensors. The real-time dynamic current and voltage values were monitored and recorded in the process of welding and the average current and voltage were obtained. The welding areas of BM were polished by abrasive paper and cleaned with ethanol to remove impurities such as oil and dust before welding. BM was placed and fixed in the water tank and the surface of BM was kept 200 mm underwater. Argon gas (99.9%) was introduced into the drainage cover as shielding gas and drainage gas, and the gas pressure was controlled at about 0.2 MPa.

Five sets of welding electrical parameters were designed before the LDU-PMIG welding experiment to gain gradually increasing LHI. The electrical parameters were peak current 260 A, 280 A, 300 A, 320 A and 340 A with the same base current 100 A, and the duty cycle of peak current was 32%. The moving speed of welding gun was defined as the welding speed, which was 14.5 mm/s.

The real average current (I_{avg}) and voltage (U_{avg}) were recorded after welding, as shown in Table 2. LHI (H) was calculated from Eq. (1), where P was the power of the welding process, v was the welding speed (14.5 mm/s), and η was the welding arc heat efficiency (0.85 for gas metal arc welding [13]). The power (P) was the average of the products of current and voltage [19], which was defined as Eq. (2), where U_j and I_j were the instantaneously measured voltage and current, and n was the number of voltage and current samples.

$$H = \eta \frac{P}{v} \tag{1}$$

$$P = \frac{1}{n} \sum_{j=1}^{j \leq n} U_j I_j \tag{2}$$

Table 2 The electrical parameters and LHI of weldments

Weldment case	1	2	3	4	5
I_{avg} (A)	152.1	158.6	164.9	170.1	177.4
U_{avg} (V)	28.0	29.1	30.1	30.4	31.2
H (J/mm)	256.2	282.4	311.4	336.7	354.6

2.2 Microstructure characterization methods

Specimens for different tests were cut from the weldments by means of wire cutting. The three directions of weldments were defined as rolling direction (RD), transverse direction (TD) and normal direction (ND), as shown in Fig. 2(a). All test surfaces of specimens were ground and polished except for tensile test specimens.

The scanning electron microscopy (SEM) specimens are shown in Fig. 2(b), and the detection areas were located in the center of WM (green zone in Fig. 2(b)). The test surfaces were etched by the etching solution, a mixture of nitric and hydrochloric acid (1:3). The phase distribution and morphology were surveyed by Zeiss (Merlin) scanning electron microscopy, and the energy dispersive spectrometer (EDS) was applied to measure the elements distribution of the detection zones. The grain structure, size, type and orientation were studied by the electron back scattering diffraction technology (EBSD), and the observation areas were situated in the same areas as that of SEM. The tensile fractures of weldments were cut down after the tensile tests and a tungsten filament scanning electron microscope (S-3700N) was applied to observe the morphology characteristics of these tensile fractures.

2.3 Mechanical performance and corrosion behaviors test methods

The microhardness value of weldments was determined by a microhardness measurer (HMV-2 T) with a load setting of 200 g and a hold time of 15 s, according to ASTM E92-82 standard. The measuring points went across the

BM, HAZ and WM with a spacing of 0.5 mm, as shown in Fig. 2(c). Tensile tests were finished by a tensile testing machine (AG-IC50kN) with the stretching velocity of 2 mm/min and the maximum load of 15 KN, according to ASTM E8M standard.

Potentiodynamic polarization (PDP) test and electrochemical impedance spectroscopy (EIS) test were widely used to explore the corrosion behaviors of various metals [1, 11, 20]. An electrochemical workstation (chi604e) was employed to finish the PDP and EIS tests of WM and BM. A conventional three-electrode cell system was chosen in the measurement. The corrosion test surfaces (6 × 6 mm, as shown in Fig. 2(d)) were used as the working electrode, a carbon cylinder as the counter electrode, and the reference electrode was Ag/AgCl electrode (saturated KCL, reference potential + 222 mV vs. standard hydrogen electrode (SHE)). NaCl solution (3.5 wt.%) was selected as the corrosion medium, considering the marine environment and its wide use in corrosion tests. Firstly, the test surfaces were immersed into NaCl solution for 30 min to finish the open circuit potential (OCP) tests, then OCP changed relatively little, which meant the relative stability between the test surface and the corrosion medium was achieved. EIS tests were carried out, with the frequency range from 100 kHz to 0.01 Hz and the amplitude of 10 mV. The software EIS Spectrum Analyser was applied to fit the impedance data with proper electrical equivalent circuit. Lastly, PDP tests were performed from -0.55 V to 0.4 V at a scanning rate of 5 mV/s. All corrosion tests were conducted at room temperature and all potentials were versus the reference potential in this paper. Each experiment was repeated three times under the same condition to make sure reproducibility.

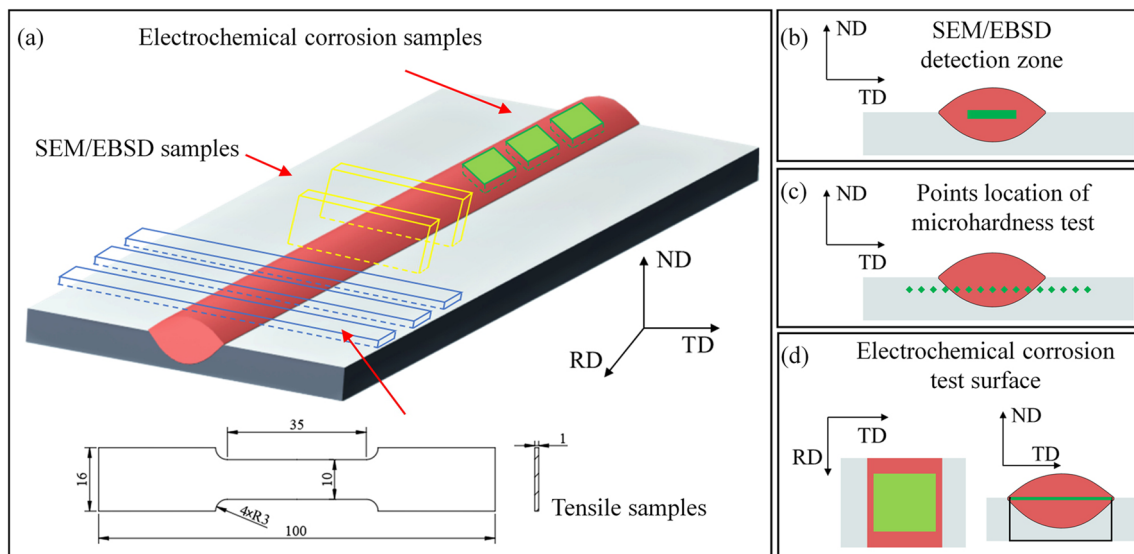


Fig. 2 Schematic diagram of samples locations and dimensions of tensile specimens (a), SEM/EBSD specimens (b), microhardness detection positions (c), electrochemical corrosion specimens (d)

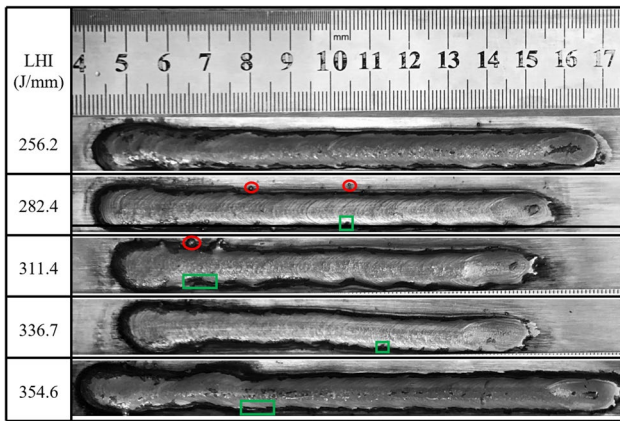


Fig. 3 Formation of LDU-PMIG weldments of different LHI

3 Results and discussions

3.1 Formation and metallography structure

The appearances of WM fabricated in different LHI are showed in Fig. 3. Tiny fish-scale ripples occurred on the surface of WM, owing to the effect of pulsed current. Some spatters (in red cycles) and undercuts (in green squares) existed in WM of different LHI. However, the formation of all underwater weldments was satisfactory by LDU-PMIG.

The microstructure and phase distribution of WM of different LHI were obtained by SEM. Figure 4(a) shows the fusion line between WM and HAZ, and HAZ was mainly composed of coarse-grained austenite. However, the HAZ of LDU-PMIG weldments was quite small because of the

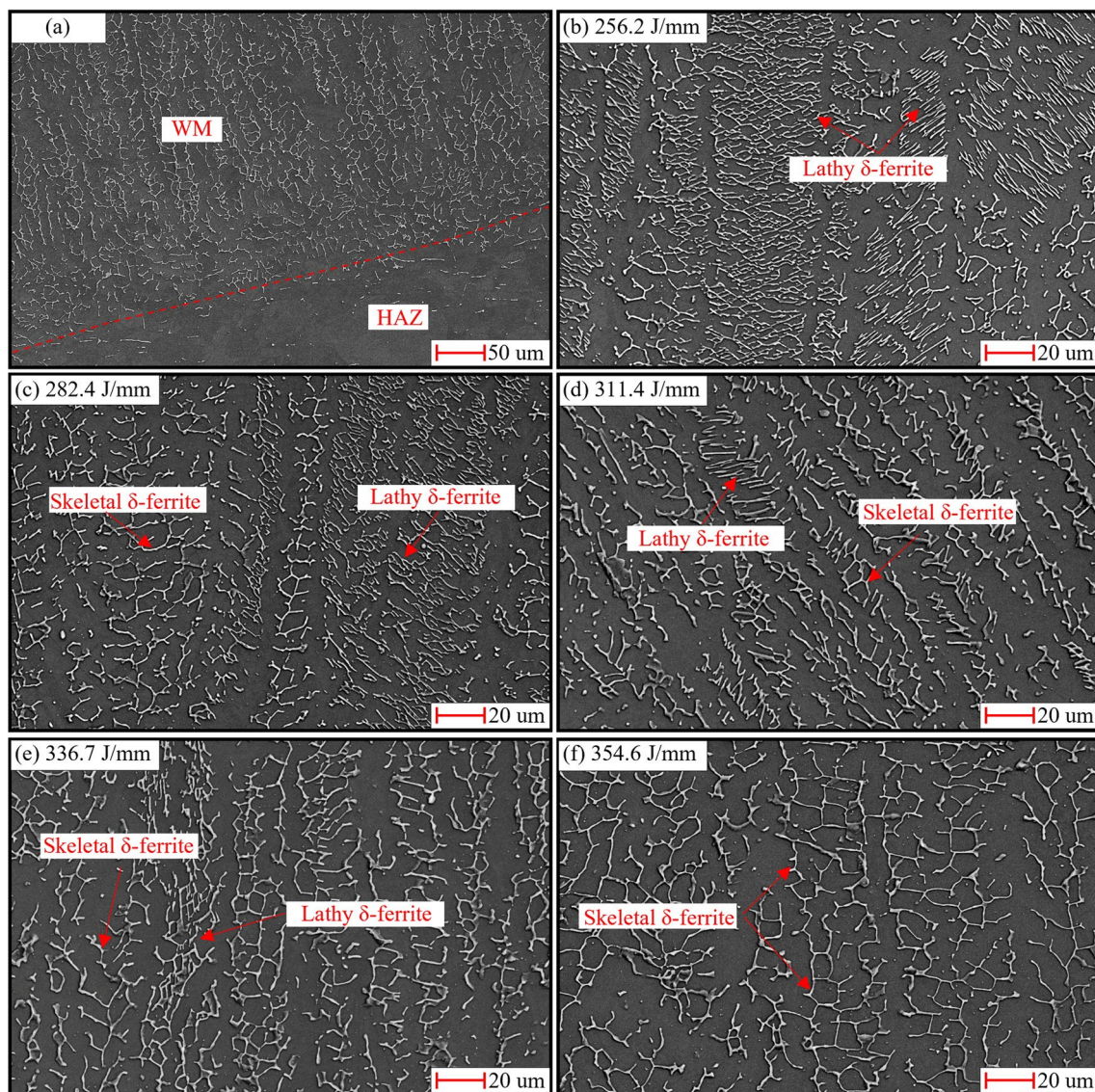
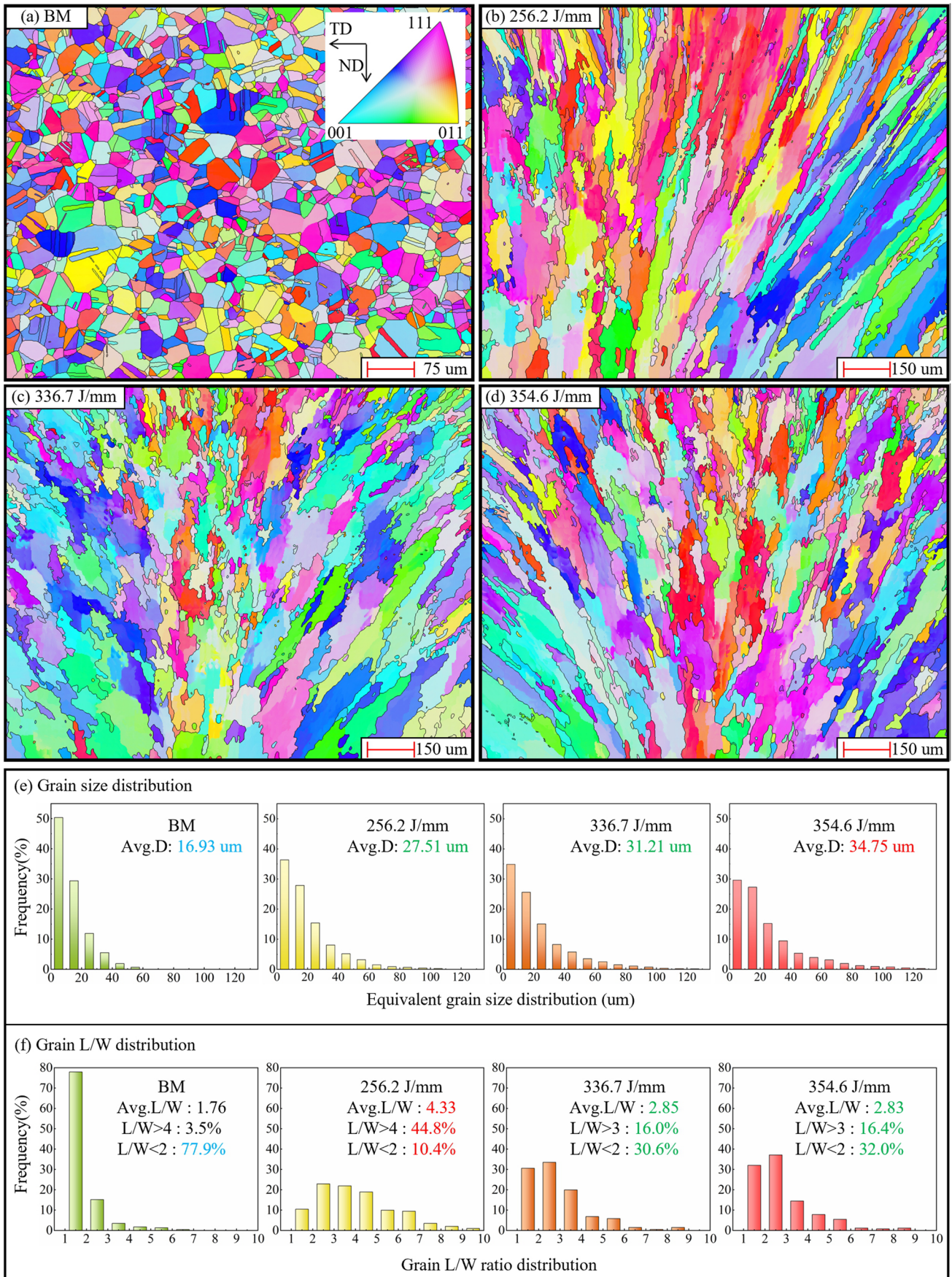


Fig. 4 Fusion line of WM (311.4 J/mm) (a), metallography structure of WM of 256.2, 282.4, 311.4, 336.7 and 354.6 J/mm (b–f)



◀**Fig. 5** IPFs of BM and WM of 256.2, 336.7 and 354.6 J/mm (a–d), grain size distribution of BM and WM (e), grain L/W distribution of BM and WM (f)

water cooling effect. The solidification mode of WM was FA mode, and the ideal solidification process was given as: $L \rightarrow L + \delta \rightarrow L + \delta + \gamma \rightarrow \delta + \gamma \rightarrow \gamma$ [21]. The rapid water cooling impeded the transformation from δ -ferrite to γ -austenite, which resulted in a small number of δ -ferrite remained in the γ matrix. Therefore, WM mainly consisted of γ -austenite and a certain amount of δ -ferrite, whose morphology was divided into two kinds: skeletal ferrite and lathy ferrite. The SEM results of WM with five different LHI are shown in Fig. 4(b–f), where the dark gray areas are austenite, while bright white areas are ferrite (marked by red arrows).

The morphology distribution of ferrite varied in WM of different LHI. Lathy ferrite content accounted for the majority, and skeletal ferrite was less when LHI was 256.2 J/mm. With the increase of LHI, the content of lathy ferrite decreased, while that of skeletal ferrite rose. The content of skeletal ferrite was clearly more than that of lathy ferrite in the WM of 354.6 J/mm. The changes in ferrite morphology were mainly determined by LHI. The cooling time increased as LHI rose, thus, the δ - γ transformation was more complete in higher LHI, which led to lathy ferrite reducing. Meanwhile, the overall ferrite content declined as LHI ascended.

3.2 Grain structure and orientation

Figure 5(a–d) shows the inverse pole figures (IPF) of BM and WM of 256.2, 336.7 and 354.6 J/mm. Figure 5(e) shows the equivalent grain size distribution of BM and WM, where the diameter of equal area circle is used to characterize the equivalent grain size. The length (L) and width (W) of grains were obtained using ImageJ software, and the ratio of length and width (L/W) distribution is shown in Fig. 5(f). Generally, grains with close length and width ($L/W < 2$) are regarded as equiaxed grains, while grains with large L/W ratio ($L/W > 4$) are columnar grains [7].

BM was mainly composed of equiaxed grains of relatively uniform size, with an average L/W ratio of 1.76. Abundant columnar grains were included in the WM of 256.2 J/mm, with an average L/W ratio of 4.33, and the content of columnar grains was as high as 44.8%, while that of equiaxed grains was only 10.4%. With LHI increasing to 336.7 J/mm, the fraction of columnar grains reduced remarkably, and equiaxed grains increased significantly compared with the WM of 256.2 J/mm. The average L/W ratio decreased to 2.85 and the content of equiaxed grains reached 30.6%. With LHI increasing to 354.6 J/mm, the fractions of columnar grains and equiaxed grains changed little compared with the WM of 336.7 J/mm. The changes of grain L/W ratio were mainly impacted by different LHI.

The cooling rate of WM was higher in lower LHI. The rapid cooling rate promoted grains to grow along the direction of heat dissipation, thus, slender columnar grains generated. As LHI increased, the cooling rate declined relatively, and equiaxed grains gradually formed, which brought about a corresponding decrease of columnar grains. However, with LHI rising further to 354.6 J/mm, the content of columnar grains reduced little, which meant the transformation from columnar grain to equiaxed grain was limited under the condition of water cooling.

The grains of BM were mainly concentrated in the range of small grains ($< 10 \mu\text{m}$), obtaining the smallest average grain size naturally. The average grain size of WM was significantly larger than BM. As LHI increased, the cooling time became enlarged and grains grew further, which resulted in the relative content of small grains declining gradually, and the average grain size increasing. The increasing rate of grain size was relatively low when LHI changed from 256.2 to 336.7 J/mm, but with further increase of LHI, the increasing rate became greater, as reflected in the grain size increasing from 31.21 to 34.75 μm . The grain size of the WM (354.6 J/mm) was coarser 26.3% than that of the WM (256.2 J/mm).

Figure 6 illustrates the pole figures of WM and BM according to EBSD, which can express austenite grain orientation distribution. The austenite grain preferred orientation of BM was $\{110\}$ with a maximum oriented density of 2.25. A single austenite preferred orientation of $\{100\}$ was observed in the WM of 256.2 J/mm, with a maximum oriented density of 5.17 due to high cooling rate in low LHI. According to the solidification principle, the grains of FCC structure grew easier along $\langle 001 \rangle$ during welding. The non-preferentially oriented grains were replaced with the faster-growing grains, which resulted in different texture density [7]. However, with LHI increasing, austenite preferred orientation of $\{111\}$ occurred in the WM of 336.7 and 354.6 J/mm. The existence of $\{111\}$ preferred orientation reflected the diversification of austenite grains orientation, which was attributed to higher LHI. As LHI rose, the time of δ - γ transformation was lengthened and atomic diffusion was promoted [7, 22].

3.3 Grain boundary and type

Grain boundaries can be divided into two kinds: the low-angle grain boundaries ($2\text{--}15^\circ$, LAGBs) and the high-angle grain boundaries ($> 15^\circ$, HAGBs) [23]. The grain boundary of BM was mainly HAGBs. The fraction of HAGBs was more than that of LAGBs in WM. As LHI increased, the content of HAGBs increased slightly, corresponding to the decrease of LAGBs, as shown in Fig. 7(c).

BM and WM of different LHI have three kinds of grain types: sub-structured grains (in yellow), recrystallized

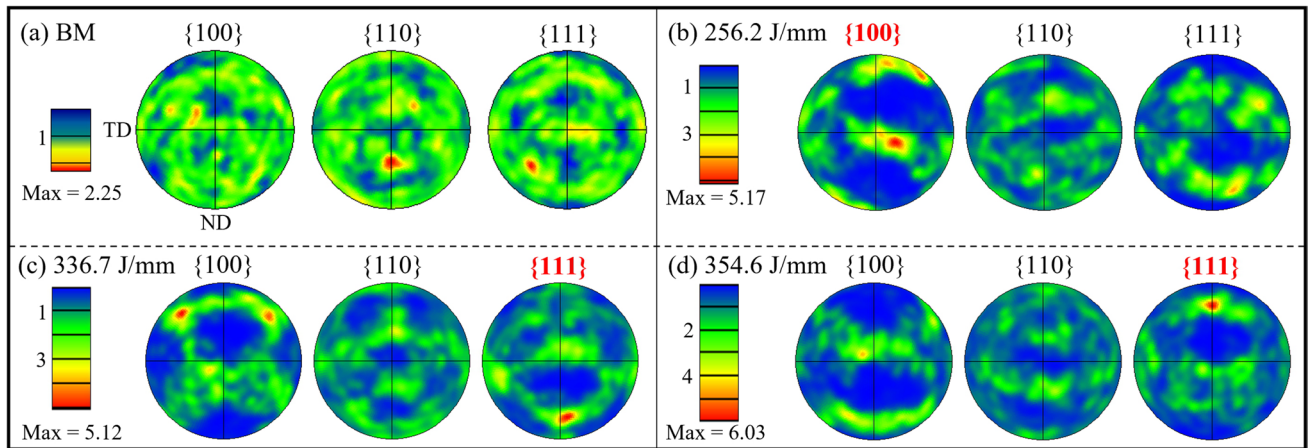


Fig. 6 Austenite grain orientation of BM (a), austenite grain orientation of WM of 256.2, 336.7 and 354.6 J/mm (b–d)

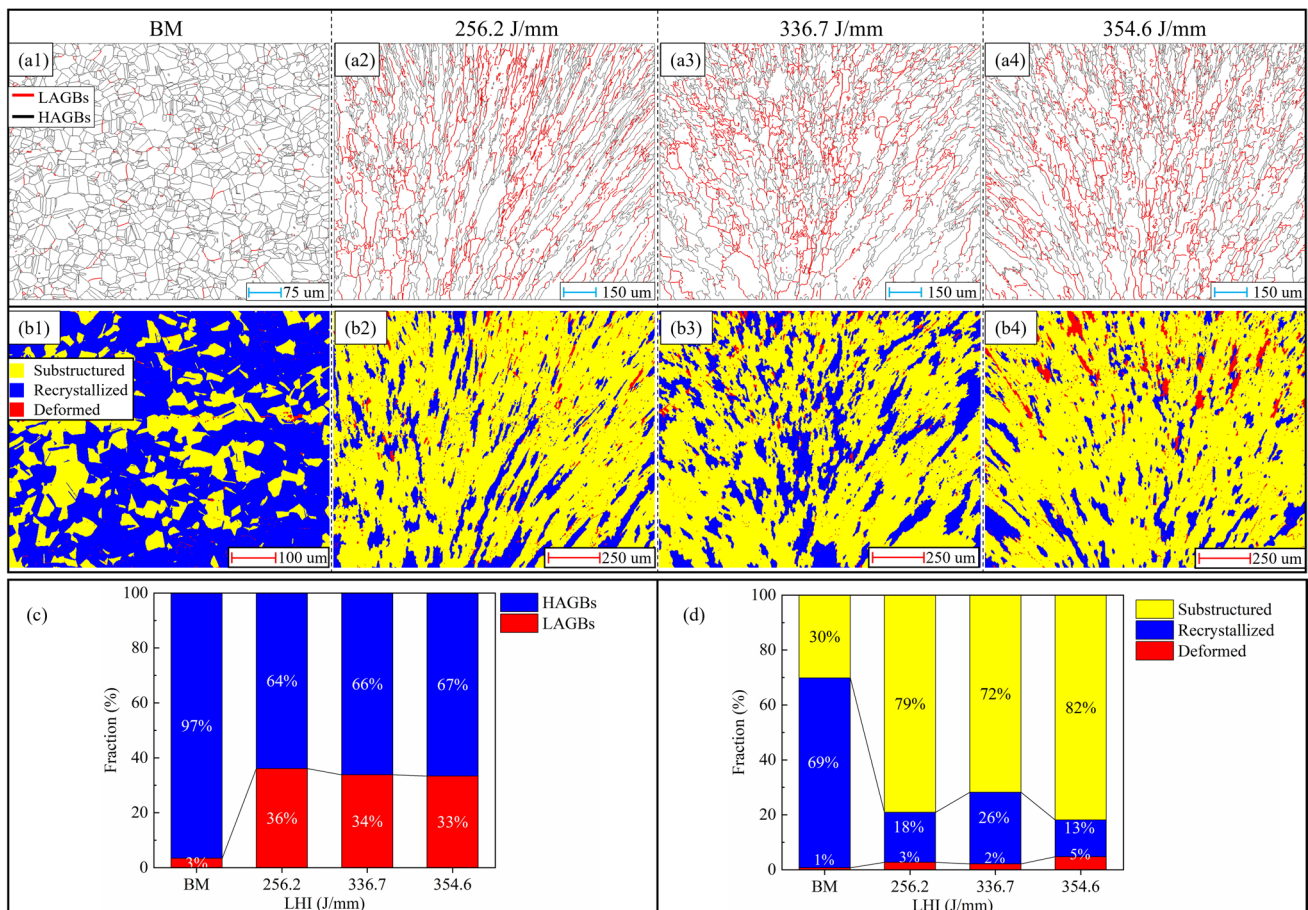


Fig. 7 Grain boundary types of BM and WM of 256.2, 336.7 and 354.6 J/mm (a1-4), grain types of BM and WM of 256.2, 336.7 and 354.6 J/mm (b1-4), distribution of grain boundary types of BM and WM (c), distribution of grain types of BM and WM (d)

grains (in blue) and deformed grains (in red), as shown in Fig. 7(b1-4). BM mainly consisted of recrystallized grains and sub-structured grains. Sub-structured grains were dominant in WM, followed by recrystallized and deformed

grains. With LHI rising, the fraction of recrystallized grains increased first and reduced then in WM, while that of deformed grains showed an opposite trend, as shown in Fig. 7(d). The WM of 336.7 J/mm had the highest content

of recrystallized grains (26%) and the lowest content of deformed grains (2%). Researches [24, 25] indicated that the potential energy released during transformation from LAGBs to HAGBs was conducive to promote deformed grains to change into recrystallized grains. With longer cooling time in higher LHI, the fraction of HAGBs increased because of ampler transformation from LAGBs to HAGBs. Thus, the content of recrystallized grains became enlarged in the WM of 336.7 J/mm, owing to longer cooling time and more released potential energy. With LHI further rising to 354.6 J/mm, higher LHI created larger thermal stress, and greater residual stress was generated in the cooling process of molten pool, as reflected in that more deformed grains were remained, and the content of recrystallized grains reduced in Fig. 7(b4). Recrystallization process can release residual stress and relieve residual strain. Therefore, the content of recrystallized grains and deformed grains may imply the changes of mechanical properties.

3.4 Mechanical performance

3.4.1 Microhardness tests

The microhardness distribution of WM of different LHI was measured, as shown in Fig. 8(a), and the indentations morphology was observed by an optical microscope, as shown in Fig. 8(c). BM had the highest microhardness compared with HAZ and WM owing to its highest content of uniform equiaxed grain and the smallest average grain size. The microhardness of HAZ gradually declined with closer to WM, and the microhardness of WM was the lowest. Figure 8(b) shows the average microhardness of WM of five different LHI.

The results showed that the microhardness of WM displayed a trend of first increasing and then decreasing, as LHI gradually ascended. The microhardness reached its maximum in the WM of 336.7 J/mm, which was 11.8% higher than that of 256.2 J/mm and reached 77.7% of BM. With LHI rising to 354.6 J/mm, the microhardness slightly decreased.

Welding heat had a greater impact on the HAZ grains closer to the WM, leading to coarser grains and microhardness decreasing. The average grain size of WM was larger, with a higher content of columnar grains, leading to the lower microhardness compared with BM and HAZ. The main reasons of microhardness increasing first were the increasing content of equiaxed grains and the diversification of grain orientation with LHI rising. Equiaxed grains have better comprehensive mechanical properties compared with columnar grains, improving the microhardness. As LHI enhanced further, the changes of equiaxed grain content and grain orientation were not significant, while the grain size was enlarged sharply, which caused microhardness decreasing in the WM of 354.6 J/mm.

3.4.2 Tensile tests and fracture morphology

Tensile tests were conducted on BM and Weldments of different LHI, and the results are shown in Fig. 9(a). All specimens were fractured at the position of WM except for BM specimens. The tensile curves of all specimens were similar, but there were remarkable differences in tensile strength and elongation, as shown in Fig. 9(b). The tensile strength and elongation of weldments showed a trend of first increasing and then decreasing with the enhancement of LHI. In

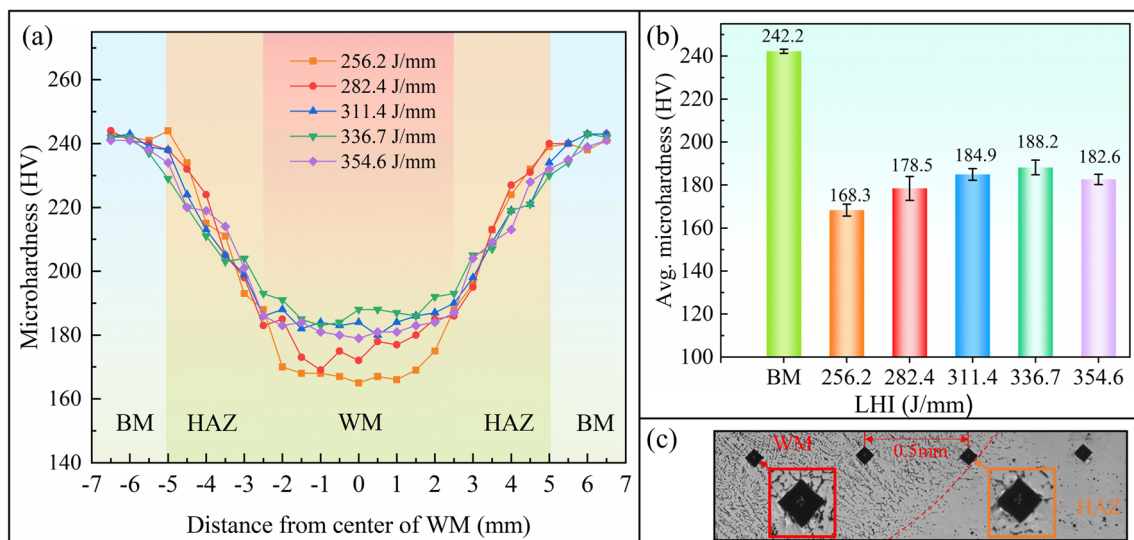


Fig. 8 Microhardness distribution of WM of different LHI (a), average microhardness of WM of different LHI (b), and indentations morphology (c)

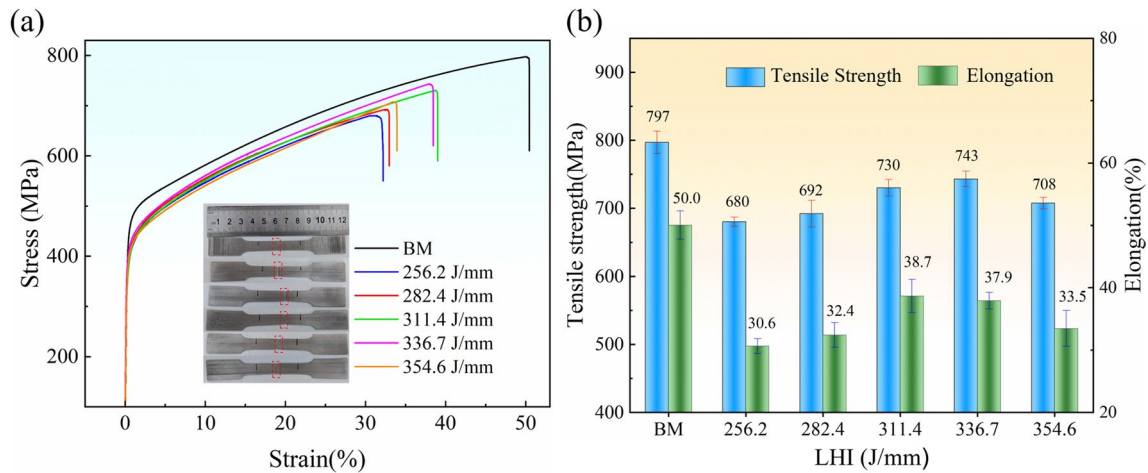


Fig. 9 Tensile curves of BM and WM (a), tensile strength and elongation of BM and WM (b)

the WM of 336.7 J/mm, the tensile strength and elongation reached their highest (743 MPa and 37.9%), which were 9.3% and 23.9% higher than that of 256.2 J/mm, and reached 93.2% and 75.8% of BM.

The fractures of BM and WM were detected, as shown in Fig. 10. The fracture of BM was mainly composed of uniformly sized dimples, exhibiting a ductile fracture mode. The equiaxed grains with uniform small size contributed to the best tensile performance of BM. In addition to dimples, there were also a large number of tearing edges and cleavage planes in the fracture of WM of low LHI (256.2 and 282.4 J/mm), which reflected the deterioration of tensile performance and exhibited a mixture of ductile and brittle fracture. Tear edges and cleavage surfaces reduced in the WM of 311.4 and 336.7 J/mm, which corresponded to the significant improvement of tensile performance. However, many tear edges occurred with LHI further rising to 354.6 J/mm, which indicated the degraded tensile performance. The fracture morphology results corresponded to the changes of tensile strength and elongation results.

The tensile performance was mainly affected by the relative content of equiaxed grains, grain preferred orientation and grain size. Equiaxed grains had better comprehensive performance than columnar grains [21], which enhanced the tensile performance. Zhan et al. [7] indicated that the {100} plane was the most prone to slip in the plastic deformation of 304L, and generally, columnar grains with clear <100> orientation characteristics were the weak areas leading to weld failure. Besides, grain coarsening caused the reduction of strength according to the principle of fine grain strengthening [26]. When LHI changed from 256.2 to 336.7 J/mm, the equiaxed grain content increased remarkably, and the grain preferred orientation became diverse, while the relative change of grain size was not significant. The influence of increasing equiaxed grain content and diversification of grain orientation was dominant, which

caused the improvement of tensile performance with LHI ascending. However, the grain size was enlarged sharply then, while the equiaxed grain content and grain preferred orientation changed little, which led to tensile performance reducing in the WM of 354.6 J/mm.

3.5 Corrosion behaviors

3.5.1 Potentiodynamic polarization tests

The PDP curves of BM and WM of different LHI were measured in 3.5 wt.% NaCl solution, as shown in Fig. 11(a). Table 3 depicts the E_{corr} (corrosion potential) and I_{corr} (corrosion current) of WM and BM. E_{corr} indicates corrosion tendency of metals, and a more negative value indicates that the metal is more inclined to be corroded. I_{corr} is a vital indicator for corrosion rate, and corrosion rate increases with I_{corr} rising, which leads to corrosion resistance declining. According to ASTM G102-89 standard, corrosion penetration rate (CR) can be determined by Eq. (3), where K is a constant, and EW and ρ are related to the material. The corrosion rate is directly proportionate to I_{corr} from Eq. (3). In order to evaluate the corrosion resistance of WM compared with BM, the CR ratios of BM and WM were calculated by using Eq. (4), where I_{BM} and I_{WM} were the I_{corr} of BM and WM, and k was the EW/ρ ratio of BM and WM. (k was approximately equal to 1 due to the close alloy elements content and density of BM and WM.)

$$CR = K \frac{EW}{\rho} i_{\text{corr}} \quad (3)$$

$$CR_{\text{vs.BM}} = k \frac{I_{\text{BM}}}{I_{\text{WM}}} \quad (4)$$

The E_{corr} of BM was higher than that of WM, which indicated that BM had a lower corrosion tendency than that of WM. Meanwhile, BM had the lowest I_{corr} , meaning the lower corrosion rate and greater corrosion resistance than all WM. Although the PDP curves of WM of different LHI had similar trends, there were differences in their corrosion behaviors. The E_{corr} of WM showed a decreasing trend, which indicated that the corrosion tendency of WM gradually became enlarged as LHI ascended. More clearly, with LHI rising, the corrosion rate of WM increased because of the augment of I_{corr} . It was worth noting that the I_{corr} of WM of 354.6 J/mm increased 20.3% than that of 336.7 J/mm, which meant that the increasing rate of I_{corr} also became enlarged in higher LHI. The changing trends of I_{corr} and corrosion resistance are shown in Fig. 11(b). The WM of the lowest LHI had the highest corrosion resistance in WM, which reached 69.9% of BM, while the corrosion resistance of WM of 354.6 J/mm was 27.3% lower than that of 256.2 J/mm and only reached 50.8% of BM.

The pitting corrosion resistance of WM was also worth noting. Pitting potential (E_p) is commonly used to measure the pitting corrosion resistance [16, 27]. E_p is the potential when stable pits generate and the current increases sharply. The materials of higher E_p exhibit greater pitting corrosion resistance. The E_p of WM was quite close without obvious change, which suggested WM of different LHI had almost consistent resistance to pitting corrosion. However, the E_p of BM was lower than that of WM, displaying worse pitting corrosion resistance. The pitting corrosion resistance of metals was largely related to the pitting resistance equivalent number (PREN), and metals of higher PREN had better pitting corrosion resistance [16, 28]. PREN mainly depended on the content of three elements (Cr, Mo and N), and PREN was calculated by Eq. (5).

$$\text{PREN} = \text{wt\%Cr} + 3.3\text{wt\%Mo} + 16\text{wt\%N} \quad (5)$$

The PRENs of WM were almost consistent due to their close elements content, which explained the consistent pitting corrosion resistance of WM of different LHI. Cr is one of the important elements in forming corrosion resistance, which plays a vital role in the generation of passivation film on the metal surface, which can effectively enhance corrosion resistance [20, 29, 30]. However, Cl ions can penetrate the passivation film [31], and gradually destroy the integrity of the passivation film, ultimately causing metal corrosion. The content of Cr in the filler metal was higher, which caused that WM had a higher Cr content than that of BM and HAZ, as shown in Fig. 12(a). Thus, the E_p of BM was slightly lower than WM.

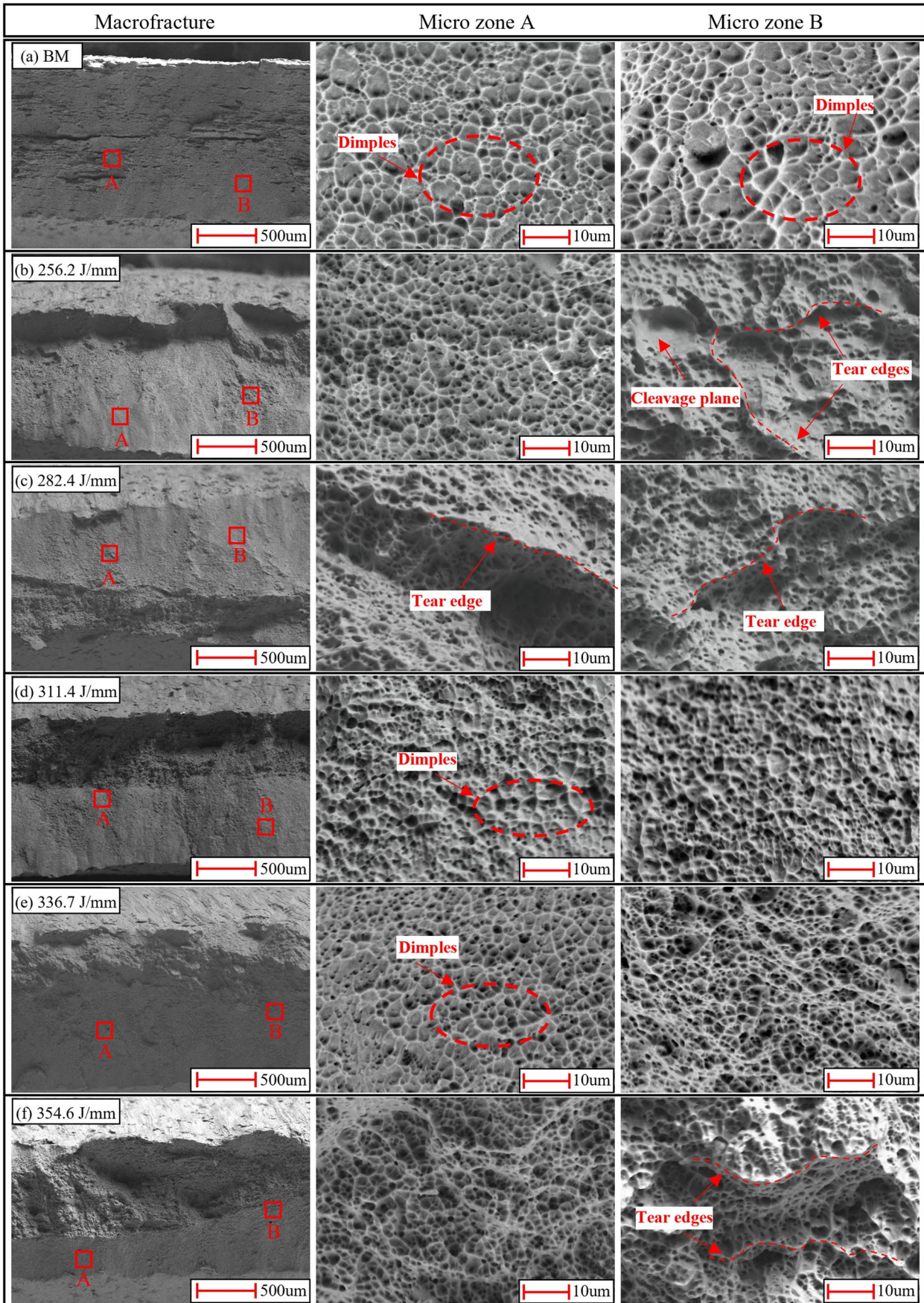
BM and WM exhibited varying degrees of passivation [1, 11], as shown in Fig. 11(a). BM had a short passivation

interval and the smallest passivation current, and there were longer passivation intervals when LHI changed from 256.2 to 336.7 J/mm. Nevertheless, the WM of 354.6 J/mm showed no significant passivation. The passivation current of WM had a rising trend, which stated that the corrosion resistance of passivated WM gradually descended with the increase of LHI.

Significantly, WM gradually formed metastable pits [32, 33] starting from 0.32 V, as shown in Fig. 11(a). The current peaks meant the break of passivation films of some local areas, which indicated the formation of metastable pits from 0.32 to 0.36 V. However, the passivation film generated again over a period of time, displaying the decline of current. The break and formation of passivation film kept cycling until stable pits occurred and the current went up sharply. The presence of metastable pits suggested that there were some defect areas on the surface of WM, which had weaker corrosion resistance.

The weak zones were the Cr-depleted areas caused by Cr precipitates, which led to intergranular corrosion in weldments. Austenitic stainless steel was inclined to form precipitation of chromium carbides ($M_{23}C_6$) [1, 34], when the solidification process passed through the temperature range of 850–600°C. The diffusion rate of Cr in austenitic grains was slower than that of C; thus, it was difficult for Cr inside grains to replenish the areas near grain boundaries, which resulted in the formation of Cr-depleted zones. The low Cr content in Cr-depleted areas was not beneficial to the generation of passivation film, which caused weak corrosion resistance. EDS surface scans were performed on the WM of 256.2, 336.7, and 354.6 J/mm, as shown in Fig. 12(b–d). The distribution of Cr was relatively uniform in the WM of 256.2 J/mm. The precipitates of Cr and C formed and areas of low Cr content appeared apparently in the WM of 354.6 J/mm. The results were consistent with the research of Li et al. [15], which suggested that rich-Cr carbides precipitated more owing to the higher LHI. The results indicated the presence of Cr-depleted zones in the SUS304 weldments of LDU-PMIG. Intergranular corrosion became more severe and the corrosion resistance declined with the increase of LHI.

Additionally, the content of ferrite had an impact on the corrosion resistance of WM. Ferrite contained a high Cr content, and the ferrite dispersed in the austenitic matrix could improve corrosion resistance [1]. With LHI enlarged, the ferrite content gradually reduced, which brought about the decrease in the corrosion resistance of WM. Moreover, the grain size could affect the corrosion resistance. Researches [35–37] have indicated that corrosion resistance improved with grain size decreasing. The grain size of WM became larger with LHI rising, which led to the reduction of corrosion resistance.



◀**Fig. 10** The fracture morphology of BM (a), and the fracture morphology of WM of 256.2, 282.4, 311.4, 336.7 and 354.6 J/mm (b–f)

After PDP tests, the surfaces of BM and WM were observed by an optical microscope, as shown in Fig. 13. The number of small corrosion pits on the surface of WM increased with LHI rising, which proposed that the corrosion resistance decreased, when LHI changed from 256.2 to 354.6 J/mm. The WM of 354.6 J/mm displayed abundant corrosion pits, with a large and deep one, which illustrated its worst corrosion resistance. The WM of 256.2 J/mm had the highest corrosion resistance. The observation results were consistent with the PDP test results.

3.5.2 Electrochemical impedance spectroscopy tests

To further investigate the corrosion behaviors of WM, the EIS tests were performed, as shown in Fig. 14. BM and WM of different LHI exhibited similar EIS curves that displayed an unfinished semicircle. The diameters of the capacitive semicircle [38] descended, which indicated the decrease of corrosion resistance. In the Bode plots, the impedance modulus value remained almost constant in the high frequency range and the phase angle approached zero, which exhibited a resistive-like behaviors [39]. From middle to low frequency, the curves seemed like a tilted straight line and the largest phase angle was achieved, which showed a behavior similar to capacitance [20].

An electrical equivalent circuit (EEC) was employed to fit the EIS data of BM and WM. The EEC consisted of a constant phase component (Q_{dl}) connected in parallel with a polarization resistor (R_p) and then in series with a solution resistor (R_s) [20, 40]. The EEC is inserted in Fig. 14(a) and the fitting results are shown in Table 4. Constant phase component (CPE) was commonly used to replace double layer capacitance to adapt to the non-ideal behaviors of capacitance in electrochemical corrosion analysis field [20, 41, 42].

$$Z_Q = \frac{1}{Y_0} (j\omega)^{-n} \quad (6)$$

CPE was mathematically described as Eq. (6), where Y_0 was the CPE parameter, n was the dispersion coefficient, and ω was the signal frequency. The value range of n was from 0 to 1. When n was 0, CPE was represented as resistance, and when n was 1, CPE was equal to capacitance. R_p depended on the properties of the passivation film, and the larger R_p meant the stronger corrosion resistance of the passivation film.

The results stated that as LHI increased, R_p gradually reduced, which meant the deterioration of corrosion resistance. The results obtained from EIS were consistent with the PDP results.

3.6 Effect of LHI on mechanical properties and corrosion behaviors

LHI had a significant impact on the mechanical properties and corrosion behaviors of SUS304 LDU-PMIG weldments, by changing the grain size, grain structure, grain orientation, phase content and Cr precipitates content. Figure 15(e) displays the changing trends of mechanical performance, elongation, microhardness and tensile strength. The mechanical performance first increased due to the transformation from columnar grain to equiaxed grain and the diversification of austenite grain orientation, and then grain coarsening caused mechanical performance decreasing. The maximum values of elongation, microhardness and tensile strength reached 75.8%, 77.7%, 93.2% of BM in the WM of 336.7 J/mm.

WM had similar pitting corrosion resistance (E_p), but corrosion rates varied in WM of different LHI, which led to different corrosion resistance. The corrosion resistance had a declining trend and the decreasing rate became enlarged with LHI enhancing, as shown in Fig. 15(d). The reduction of corrosion resistance was mainly attributed to more Cr precipitates content, less ferrite content and coarser grains, caused by higher LHI. Thus, the WM of 256.2 J/mm obtained the highest corrosion resistance, while corrosion resistance of the WM of 354.6 J/mm reduced sharply, 27.3% less than that of 256.2 J/mm.

The average value of tensile strength, elongation and microhardness was regarded as the average mechanical performance of WM in this paper. The average mechanical performance and corrosion resistance versus the WM of 256.2 J/mm are displayed in Fig. 15(f). The WM of 256.2 J/mm had the best corrosion resistance and worst mechanical performance compared with other weldments. The corrosion resistance and mechanical performance of the WM of 354.6 J/mm fell dramatically compared with other weldments. A significant balance of mechanical performance and corrosion resistance was achieved in the WM of 336.7 J/mm.

The findings and results of other researches were compared with the conclusions as mentioned above. To obtain better mechanical performance and corrosion resistance, proper ranges of LHI were studied by researchers. The changing trends of mechanical performance of some researches are displayed in Fig. 16(a). Li et al. [12] found that the tensile strength of E40 underwater wet FCAW weldments improved as LHI rose, and it was attributed to the solid solution strengthening of alloying elements. However, Gao et al. [14] reported the tensile strength of S355 underwater wet weldments decreased with LHI increasing. Grain coarsening and increasing diffusive hydrogen made the tensile strength reduce. Zhan et al. [7] found the tensile strength of 304 fiber-diode hybrid laser weldments kept increasing before a certain LHI, which was mainly attributed to the generation of equiaxed grains. Because of grain coarsening, the tensile strength

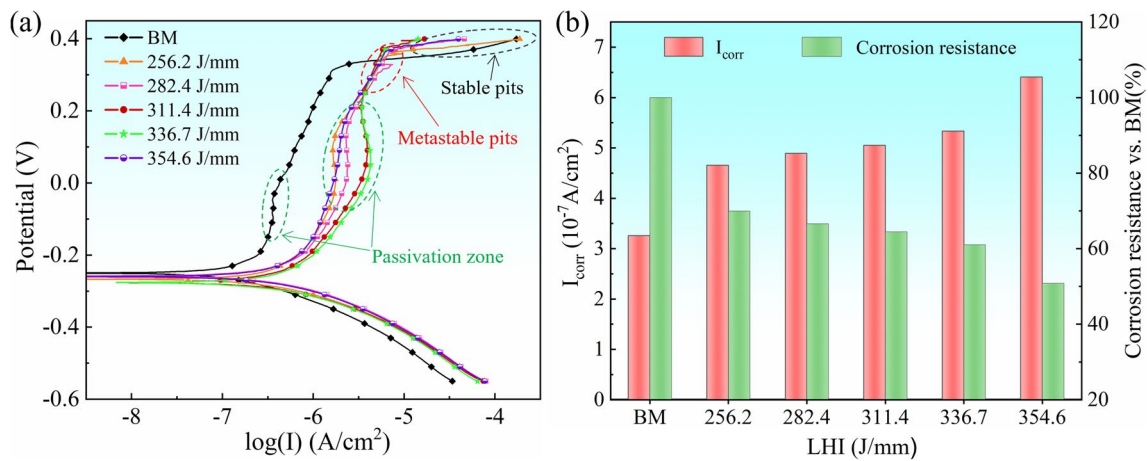


Fig. 11 PDP curves of BM and WM (a), I_{corr} of BM and WM and corrosion resistance of WM vs. BM (b)

Table 3 Electrochemical parameter results of PDP tests

LHI (J/mm)	BM	256.2	282.4	311.4	336.7	354.6
E_{corr} (V)	-0.250	-0.267	-0.258	-0.276	-0.276	-0.260
I_{corr} (10^{-7} A/cm ²)	3.256	4.656	4.892	5.053	5.333	6.406
E_p (V)	0.330	0.365	0.365	0.365	0.370	0.365
CR _{vs. BM} (%)	100	69.9	66.6	64.4	61.0	50.8

reduced after the certain LHI. To sum up, many factors are able to influence the mechanical performance of weldments. Therefore, it is greatly possible to find that the mechanical performance can reach its maximum in a proper range of LHI owing to the comprehensive effect of two or more factors. In this study, the maximum of mechanical performance was observed in the LHI range from 256.2 to 354.6 J/mm. The changing trend of this study (red curve in Fig. 16(a)) was similar with the results of fiber-diode hybrid laser welding (black curve in Fig. 16(a)). In these researches [7, 14], the reduction of mechanical performance was attributed to grain coarsening, which was also the main reason of mechanical performance decreasing in this study. The close tensile strength was achieved in other LDUW study. Fu et al. [21] reported the tensile strength of 304 underwater laser weldments reached 670 MPa, which was close to the value of this study under the condition of similar LHI.

Figure 16(b) shows the changing trends of corrosion resistance of weldments in different studies. Singh et al. [10] found less depletion of chromium in low LHI was beneficial to the improvement of corrosion resistance of martensitic stainless steel (AISI410) weldments. Sun et al. [18] reported that with LHI rising, the corrosion resistance of S32101 underwater dry FCAW weldments reduced. However, Ma et al. [11] found that the corrosion resistance of 2205 underwater wet FCAW weldments kept increasing as

LHI rose. In fact, the material of weldment is one of vital factors influencing the changing trend of corrosion resistance. For SUS304 weldments, the Cr-depleted areas tended to be corroded, which resulted in the decrease of overall corrosion resistance. Less depletion of Cr was the main reason for the improvement of corrosion resistance in this study, and the research [10] had the similar results.

When the mechanical performance of SUS304 LDU-PMIG weldments reached its maximum, its corrosion resistance declined due to the increasing LHI. LHI should be taken into consideration to meet the requirement of both mechanical performance and corrosion resistance in the real welding application. New techniques may be carried into the process of LDUW to enhance both mechanical performance and corrosion resistance in the future research.

4 Conclusions

For further application in underwater installation and maintenance field, this paper investigated the influence of linear heat input on microstructure, mechanical properties and corrosion behaviors of SUS304 weldments fabricated by local dry underwater pulsed metal inert-gas welding. Some remarkable conclusions were gained as follows:

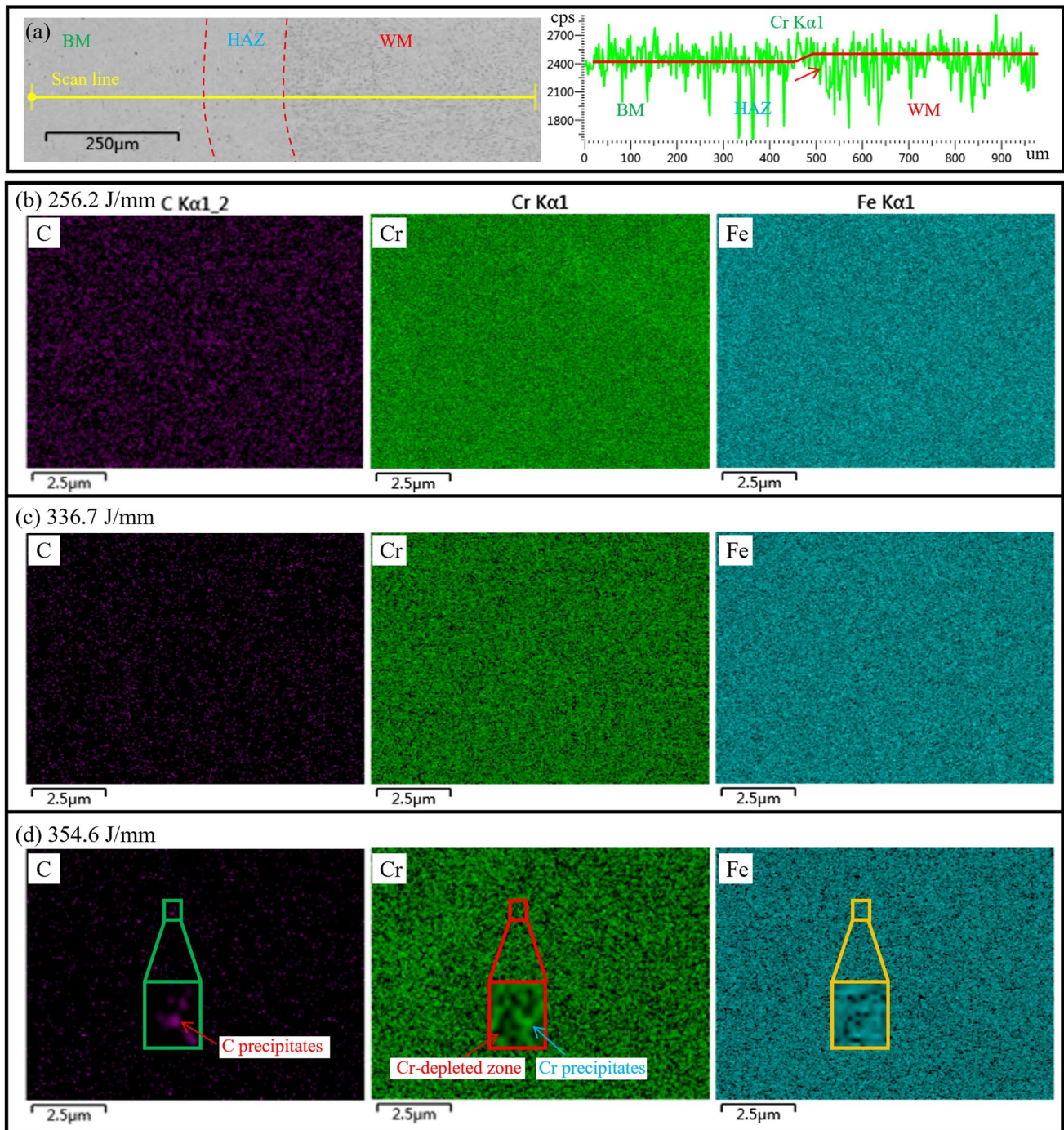


Fig. 12 Line scan of BM and WM (a), and surface scan of WM of 256.2, 336.7, and 354.6 J/mm (b–d)

- (1) As heat input of welding rose, the morphology of ferrite changed from lath to skeleton and the total amount of ferrite reduced in the weldments. The content of equiaxed grains ascended remarkably, the grain size of weldments became greater and the increasing rate of grain size was enlarged. The grain preferred orientation became diverse due to longer cooling time.
- (2) With heat input increasing, the mechanical performance increased first, and decreased after heat input reached 336.7J/mm. The primary reasons of mechanical performance improvement were the transformation from columnar grain to equiaxed grain and the diversification of austenite grain orientation, and the reduction

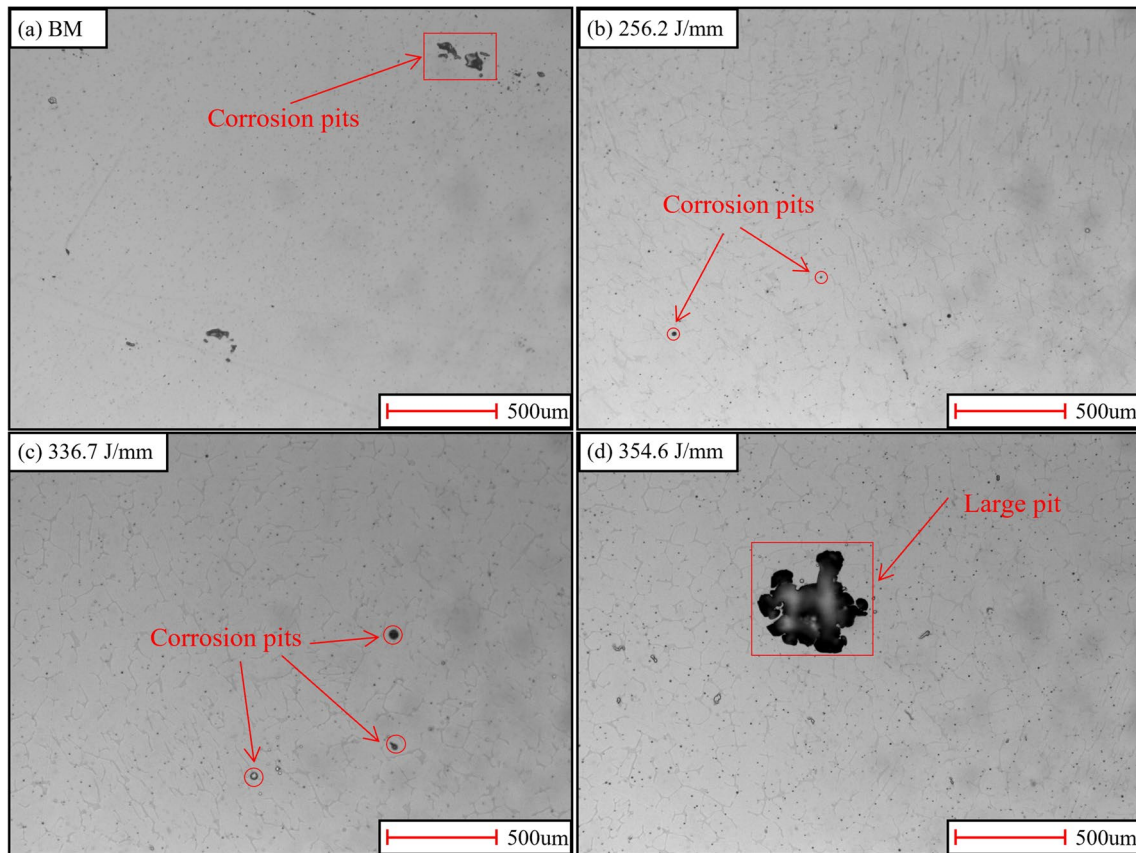


Fig. 13 Corrosion surfaces of BM after PDP tests (a), corrosion surfaces of WM of 256.2, 336.7, and 354.6 J/mm after PDP tests (b–d)

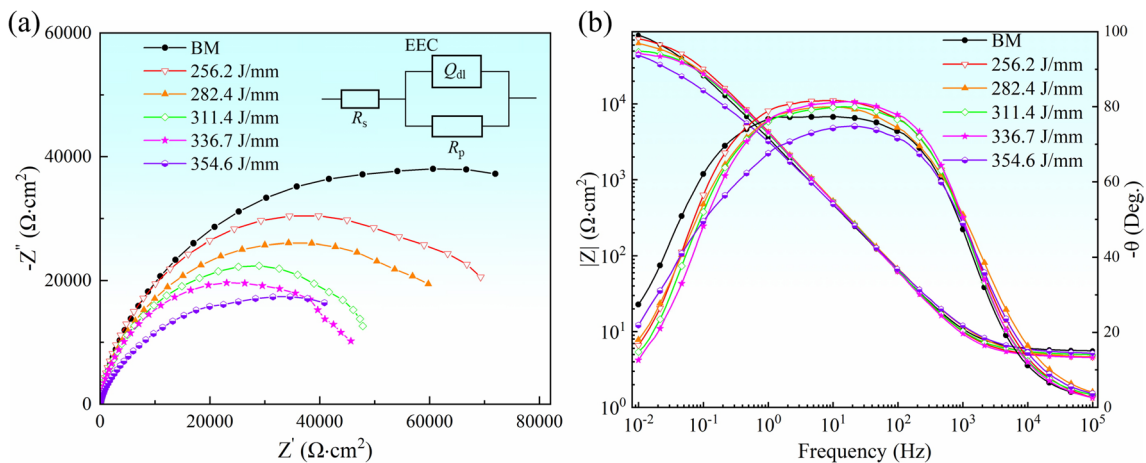


Fig. 14 Nyquist plots of electrochemical impedance of BM and WM (a), Bode plots of electrochemical impedance of BM and WM (b)

of mechanical performance was attributed to the grain coarsening.

- (3) The corrosion resistance reduced with heat input increasing, which was attributed to more Cr precipitates content, less ferrite content and coarser grains.

The corrosion resistance of weldments was lower than that of base metal.

- (4) Low heat input was preferred to achieve high corrosion resistance for SUS304 weldments, and both mechanical performance and corrosion resistance began to fall

Table 4 Fitting results of EIS data

LHI (J/mm)	BM	256.2	282.4	311.4	336.7	354.6
$R_s (\Omega \cdot \text{cm}^2)$	5.63	4.8	4.9	5.14	4.69	5.17
$Y_0 (10^{-5} \Omega^{-1} \cdot \text{s}^{-n} \cdot \text{cm}^{-2})$	5.85	4.5	4.91	4.88	4.61	7.21
n	0.87	0.91	0.88	0.9	0.91	0.83
$R_p (\Omega \cdot \text{cm}^2)$	94,366.8	74,332.8	66,139.2	52,398	47,332.8	37,011.6

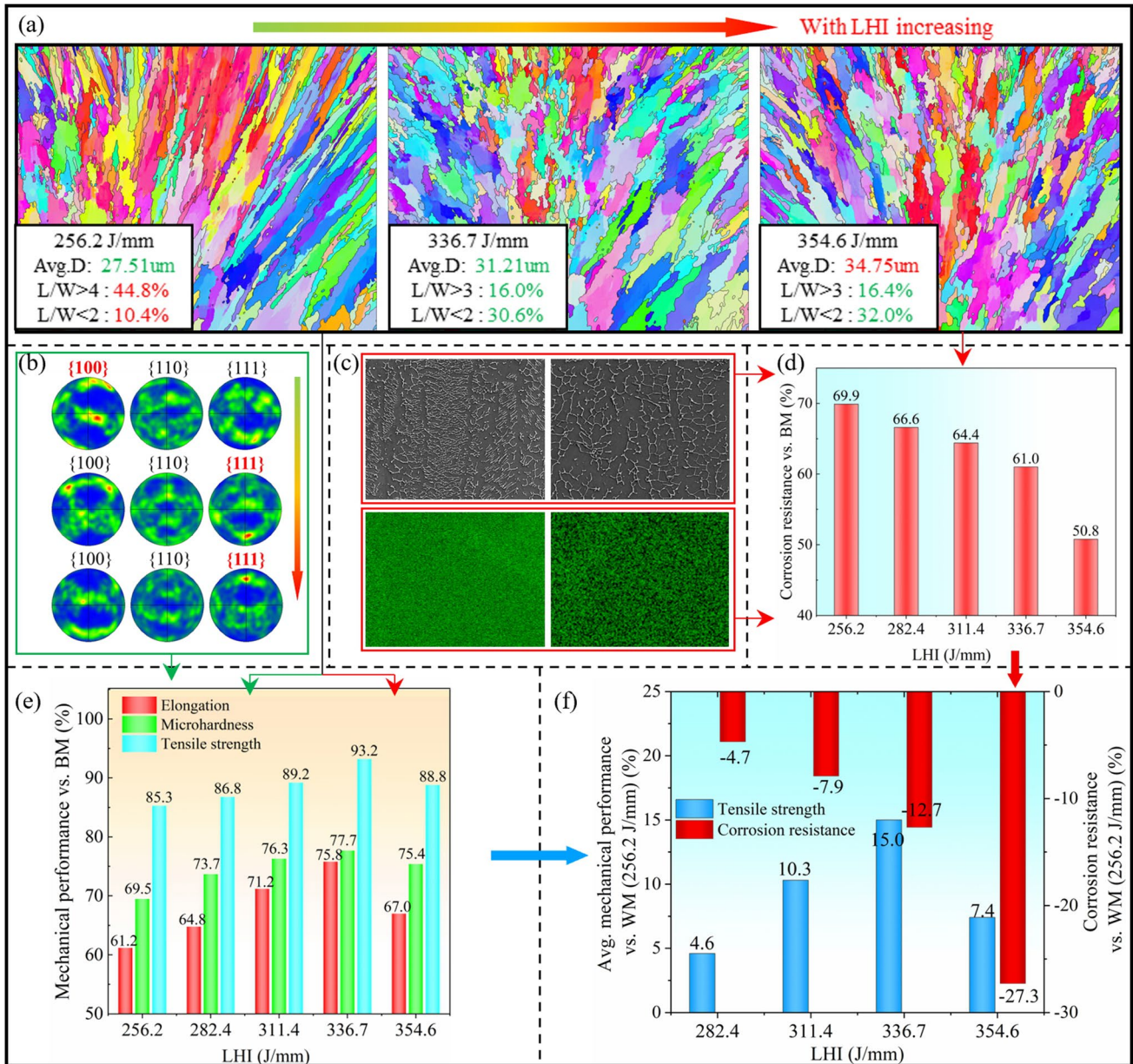


Fig. 15 Schematic diagram of effect of LHI on mechanical performance and corrosion resistance. The grain structure of WM (a), the grain orientation of WM (b), the phase distribution and EDS of WM

(c), the corrosion resistance of WM vs. BM (d), the mechanical performance of WM (e), the mechanical performance and corrosion resistance of WM vs. WM (256.2 J/mm) (f)

remarkably, when heat input reached a certain value (336.7 J/mm). The weldments of 336.7 J/mm achieved

a meaningful balance between mechanical performance and corrosion resistance.

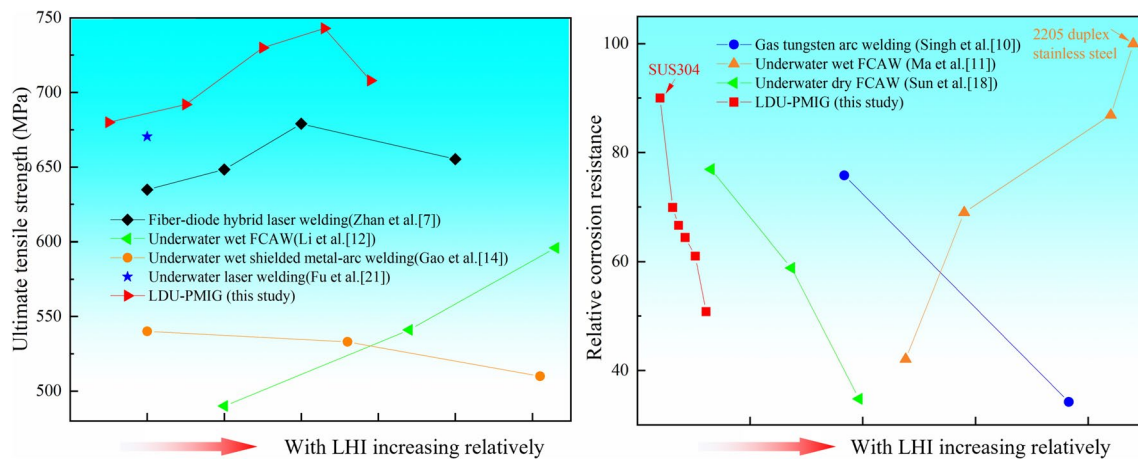


Fig. 16 Changing trends of mechanical performance with LHI increasing in different researches (a), changing trends of corrosion resistance with LHI increasing in different researches (b)

Acknowledgements The authors are thankful to editors and reviewers.

Author contribution Zhenmin Wang: conceptualization; funding acquisition; review and editing the manuscript; supervision. Bin Zhang: original draft preparation; investigation and summary of partial content in the manuscript; review. Haipeng Liao: conceptualization; experiment; review; supervision. Xiangmiao Wu: review; methodology. Jiyu Tian: writing; review; supervision; methodology. Qin Zhang: review and editing.

Funding This work was supported by the Science and Technology Program of Guangdong Province (Grant number 2021B1515420006, 2021B1515120026), National Natural Science Foundation of China (Grant number U23A20625, U2141216, 52375334, 52305357), the National Key Research and Development Project of China (Grant number 2023YFB3407703), and the Shenzhen Science and Technology Plan (Grant number KJZD20230923114614029), National Defense Key Laboratory Fund Project (Grant number 61420052022WD011).

Data availability The datasets generated and/or analyzed during the current study are available from the corresponding author on reasonable request.

Declarations

Ethics approval The authors declare that this manuscript was not submitted to more than one journal for simultaneous consideration. Also, the submitted work was original and has not been published elsewhere in any form or language.

Consent to participate and publish The authors declare that they participated in this paper willingly and the authors declare to consent to the publication of this paper.

Informed consent All the authors listed have approved the manuscript that is enclosed.

Competing interests The authors declare no competing interests.

References

- Mirshekari GR, Tavakoli E, Atapour M, Sadeghian B (2014) Microstructure and corrosion behavior of multipass gas tungsten arc welded 304L stainless steel. *Mater Design* 55:905–911. <https://doi.org/10.1016/j.matdes.2013.10.064>
- Kalyankar V, Bhoskar A (2021) Influence of torch oscillation on the microstructure of Colmonoy 6 overlay deposition on SS304 substrate with PTA welding process. *Metallurgical Research & Technology* 118:406. <https://doi.org/10.1051/metal/2021045>
- Li J, Sun Q, Liu Y, Zhen Z, Sun Q, Feng J (2020) Melt flow and microstructural characteristics in beam oscillation superimposed laser welding of 304 stainless steel. *J Manuf Process* 50:629–637. <https://doi.org/10.1016/j.jmapro.2019.12.053>
- Kumar S, Shahi A (2011) Effect of heat input on the microstructure and mechanical properties of gas tungsten arc welded AISI 304 stainless steel joints. *Mater Design* 32:3617–3623. <https://doi.org/10.1016/j.matdes.2011.02.017>
- Liao HP, Zhang WX, Li XY, Pei K, Lin SB, Tian JY, Wang ZM (2022) Numerical simulation and experimental verification of droplet transfer during local dry underwater MIG welding process of SUS304. *J Mater Res Technol* 21:1960–1973. <https://doi.org/10.1016/j.jmrt.2022.10.040>
- Liao HP, Zhang WX, Li XY, Pei K, Lin SB, Tian JY, Wang ZM (2022) Effect of pulse current on droplet transfer behavior and weld formation of 304 stainless steel in local dry underwater pulse MIG welding. *Int J Adv Manuf Tech* 122:869–879. <https://doi.org/10.1007/s00170-022-09938-y>
- Zhan XH, Zhang JH, Wang JF, Wang LL, Li X, Zhao YQ (2022) Microstructure characteristics and mechanical properties of fiber-diode hybrid laser welded 304 austenitic stainless steel. *Mat Sci Eng A-Struct* 854:143884. <https://doi.org/10.1016/j.msea.2022.143884>
- Kose C (2022) Effect of heat input and post weld heat treatment on the texture, microstructure and mechanical properties of laser beam welded AISI 317L austenitic stainless steel. *Mat Sci Eng A-Struct* 855:143966. <https://doi.org/10.1016/j.msea.2022.143966>
- Kumar GS, Saravanan S, Raghukandan K (2021) Effect of heat input on microstructure and mechanical properties of laser welded

- dissimilar grade nickel alloys. *Optik* 248:168106. <https://doi.org/10.1016/j.ijleo.2021.168106>
10. Singh M, Shahi AS, Singh D (2021) Influence of heat input on the pitting corrosion and tensile behavior of GTA welded martensitic stainless steel (AISI410 SS) joints. *Mater Today-Proc* 46:10282–10287. <https://doi.org/10.1016/j.matpr.2020.12.187>
 11. Ma Q, Luo CC, Liu SX, Li HL, Wang PF, Liu D, Lei YC (2021) Investigation of arc stability, microstructure evolution and corrosion resistance in underwater wet FCAW of duplex stainless steel. *J Mater Res Technol* 15:5482–5495. <https://doi.org/10.1016/j.jmrt.2021.11.023>
 12. Li HL, Liu D, Yan YT, Guo N, Liu YB, Feng JC (2018) Effects of heat input on arc stability and weld quality in underwater wet flux-cored arc welding of E40 steel. *J Manuf Process* 31:833–843. <https://doi.org/10.1016/j.jmapro.2018.01.013>
 13. Di X, Ji S, Cheng F, Wang D, Cao J (2015) Effect of cooling rate on microstructure, inclusions and mechanical properties of weld metal in simulated local dry underwater welding. *Mater Design* 88:505–513. <https://doi.org/10.1016/j.matdes.2015.09.025>
 14. Gao WB, Wang DP, Cheng FJ, Di XJ, Deng CY, Xu W (2016) Microstructural and mechanical performance of underwater wet welded S355 steel. *J Mater Process Tech* 238:333–340. <https://doi.org/10.1016/j.jmatprotec.2016.07.039>
 15. Li JG, Li H, Liang Y, Liu PL, Yang LJ, Wang YW (2020) Effects of heat input and cooling rate during welding on intergranular corrosion behavior of high nitrogen austenitic stainless steel welded joints. *Corros Sci* 166:108445. <https://doi.org/10.1016/j.corsci.2020.108445>
 16. Han LH, Han T, Chen GX, Wang BY, Sun JB, Wang Y (2021) Influence of heat input on microstructure, hardness and pitting corrosion of weld metal in duplex stainless steel welded by key-hole-TIG. *Mater Charact* 175:111052. <https://doi.org/10.1016/j.matchar.2021.111052>
 17. Zhang JH, Hu K, Zhao JY, Duan SY, Zhan XH (2022) Effect of heat input on microstructure and corrosion resistance in heat affected zone of 304 stainless steel joint by laser welding. *Mater Today Commun* 30:103054. <https://doi.org/10.1016/j.mtcomm.2021.103054>
 18. Sun K, Zeng M, Shi YH, Hu Y, Shen XQ (2018) Microstructure and corrosion behavior of S32101 stainless steel underwater dry and wet welded joints. *J Mater Process Tech* 256:190–201. <https://doi.org/10.1016/j.jmatprotec.2018.02.018>
 19. Scotti A, Batista MA, Eshagh M (2022) Inaccuracy in arc power calculation through a product of voltage and current averages. *J Braz Soc Mech Sci Eng* 44:11. <https://doi.org/10.1007/s40430-021-03317-6>
 20. Luo H, Li ZM, Mingers AM, Raabe D (2018) Corrosion behavior of an equiatomic CoCrFeMnNi high-entropy alloy compared with 304 stainless steel in sulfuric acid solution. *Corros Sci* 134:131–139. <https://doi.org/10.1016/j.corsci.2018.02.031>
 21. Fu YL, Guo N, Cheng Q, Zhang D, Feng JC (2020) Underwater laser welding for 304 stainless steel with filler wire. *J Mater Res Technol* 9:15648–15661. <https://doi.org/10.1016/j.jmrt.2020.11.029>
 22. Chen R, Jiang P, Shao XY, Mi GY, Wang CM (2018) Enhancement of fatigue resistance for 316L welds produced by magnetic field assisted laser-MIG hybrid welding. *J Mater Process Tech* 254:114–123. <https://doi.org/10.1016/j.jmatprotec.2017.11.030>
 23. Gholizadeh R, Shibata A, Tsuji N (2020) Grain refinement mechanisms in BCC ferritic steel and FCC austenitic steel highly deformed under different temperatures and strain rates. *Mat Sci Eng A-Struct* 790:139708. <https://doi.org/10.1016/j.msea.2020.139708>
 24. Wang YJ, Liu WH, Wang DQ, Yu C, Xu JJ, Lu H, Chen JM (2021) Simultaneously enhanced strength and ductility of TIG welds in Inconel 718 super-alloy via ultrasonic pulse current. *Mat Sci Eng A-Struct* 807:140894. <https://doi.org/10.1016/j.msea.2021.140894>
 25. Li J, Nie JF, Xu QF, Zhao K, Liu XF (2020) Enhanced mechanical properties of a novel heat resistant Al-based composite reinforced by the combination of nano-aluminides and submicron TiN particles. *Mat Sci Eng A-Struct* 770:138488. <https://doi.org/10.1016/j.msea.2019.138488>
 26. Zhao MM, Wu HY, Lu JN, Sun GS, Du LX (2022) Effect of grain size on mechanical property and corrosion behavior of a metastable austenitic stainless steel. *Mater Charact* 194:112360. <https://doi.org/10.1016/j.matchar.2022.112360>
 27. Wang CM, Yu Y, Yu JX, Zhang Y, Zhao Y, Yuan QW (2020) Microstructure evolution and corrosion behavior of dissimilar 304/430 stainless steel welded joints. *J Manuf Process* 50:183–191. <https://doi.org/10.1016/j.jmapro.2019.12.015>
 28. Zhang ZQ, Jing HY, Xu LY, Han YD, Zhao L, Zhang JL (2017) Influence of microstructure and elemental partitioning on pitting corrosion resistance of duplex stainless steel welding joints. *Appl Surf Sci* 394:297–314. <https://doi.org/10.1016/j.apsusc.2016.10.047>
 29. Kalyankar V, Bhoskar A, Deshmukh D, Patil S (2022) On the performance of metallurgical behaviour of Stellite 6 cladding deposited on SS316L substrate with PTAW process. *Can Metall Q* 61:130–144. <https://doi.org/10.1080/00084433.2022.2031681>
 30. Bhoskar A, Kalyankar V, Deshmukh D (2023) Metallurgical characterisation of multi-track Stellite 6 coating on SS316L substrate. *Can Metall Q* 62:665–677. <https://doi.org/10.1080/00084433.2022.2149009>
 31. Zhang B, Wang J, Wu B, Guo XW, Wang YJ, Chen D, Zhang YC, Du K, Oguzie EE, Ma XL (2018) Unmasking chloride attack on the passive film of metals. *Nat Commun* 9:2559. <https://doi.org/10.1038/s41467-018-04942-x>
 32. Pradhan SK, Bhuyan P, Mandal S (2019) Influence of the individual microstructural features on pitting corrosion in type 304 austenitic stainless steel. *Corros Sci* 158:108091. <https://doi.org/10.1016/j.corsci.2019.108091>
 33. Sun M, Luo M, Lu C, Liu TW, Wu YP, Jiang LZ, Li J (2015) Effect of Alloying Tin on the Corrosion Characteristics of Austenitic Stainless Steel in Sulfuric Acid and Sodium Chloride Solutions. *Acta Metall Sin-Engl* 28:1089–1096. <https://doi.org/10.1007/s40195-015-0299-4>
 34. Garcia C, de Tiedra MP, Blanco Y, Martin O, Martin F (2008) Intergranular corrosion of welded joints of austenitic stainless steels studied by using an electrochemical minicell. *Corros Sci* 50:2390–2397. <https://doi.org/10.1016/j.corsci.2008.06.016>
 35. Ralston KD, Birbilis N, Davies CHJ (2010) Revealing the relationship between grain size and corrosion rate of metals. *Scripta Mater* 63:1201–1204. <https://doi.org/10.1016/j.scriptamat.2010.08.035>
 36. Gollapudi S (2012) Grain size distribution effects on the corrosion behaviour of materials. *Corros Sci* 62:90–94. <https://doi.org/10.1016/j.corsci.2012.04.040>
 37. Zhang WJ, Liu FG, Liu LX, Li QG, Liu L, Liu FC, Huang CP (2022) Effect of grain size and distribution on the corrosion behavior of Y2O3 dispersion-strengthened 304 stainless steel. *Mater Today Commun* 31:103723. <https://doi.org/10.1016/j.mtcomm.2022.103723>
 38. Della Rovere CA, Alano JH, Silva R, Nascente PAP, Otubo J, Kuri SE (2012) Characterization of passive films on shape memory stainless steels. *Corros Sci* 57:154–161. <https://doi.org/10.1016/j.corsci.2011.12.022>

39. Fajardo S, Bastidas DM, Criado M, Bastidas JM (2014) Electrochemical study on the corrosion behaviour of a new low-nickel stainless steel in carbonated alkaline solution in the presence of chlorides. *Electrochim Acta* 129:160–170. <https://doi.org/10.1016/j.electacta.2014.02.107>
40. Marcelin S, Pebere N, Regnier S (2013) Electrochemical characterisation of a martensitic stainless steel in a neutral chloride solution. *Electrochim Acta* 87:32–40. <https://doi.org/10.1016/j.electacta.2012.09.011>
41. Wang Y, Qiu YB, Chen ZY, Guo XP (2017) Corrosion of polypyrrole: kinetics of chemical and electrochemical processes in NaOH solutions. *Corros Sci* 118:96–108. <https://doi.org/10.1016/j.corsci.2017.01.023>
42. Cui ZY, Wang LW, Ni HT, Hao WK, Man C, Chen SS, Wang X, Liu ZY, Li XG (2017) Influence of temperature on the electrochemical and passivation behavior of 2507 super duplex stainless steel in simulated desulfurized flue gas condensates. *Corros Sci* 118:31–48. <https://doi.org/10.1016/j.corsci.2017.01.016>

Publisher's Note Springer Nature remains neutral with regard to jurisdictional claims in published maps and institutional affiliations.

Springer Nature or its licensor (e.g. a society or other partner) holds exclusive rights to this article under a publishing agreement with the author(s) or other rightsholder(s); author self-archiving of the accepted manuscript version of this article is solely governed by the terms of such publishing agreement and applicable law.